Journal of Catalysis 352 (2017) 282–292

Contents lists available at ScienceDirect

Journal of Catalysis

journal homepage: www.elsevier.com/locate/jcat

Insights into the active sites of ordered mesoporous cobalt oxide catalysts for the total oxidation of *o*-xylene

Shaohua Xie, Yuxi Liu *, Jiguang Deng *, Jun Yang, Xingtian Zhao, Zhuo Han, Kunfeng Zhang, Hongxing Dai *

Beijing Key Laboratory for Green Catalysis and Separation, Key Laboratory of Beijing on Regional Air Pollution Control, Key Laboratory of Advanced Functional Materials, Education Ministry of China, and Laboratory of Catalysis Chemistry and Nanoscience, Department of Chemistry and Chemical Engineering, College of Environmental and Energy Engineering, Beijing University of Technology, Beijing 100124, China

ARTICLE INFO

Article history:
Received 13 February 2017
Revised 24 May 2017
Accepted 25 May 2017

Keywords:
Mesoporous transition metal oxides
Cobalt monoxide
Divalent cobalt species
O-xylene oxidation
Oxygen activation ability

ABSTRACT

Cobalt oxide is a typical transition metal oxide that exhibits high catalytic activity for the total oxidation of volatile organic compounds. In this study, a reduction process in a glycerol solution was adopted to generate mesoporous CoO (meso-CoO) or CoO_x (meso-CoO_x) from mesoporous Co_3O_4 (meso-Co_3O_4). The obtained samples were rich in Co^{2+} species and exhibited high catalytic activity for *o*-xylene oxidation. The meso-CoO_x sample with the largest surface Co^{2+} amount performed the best: The *o*-xylene conversion at 240 °C was 83%, and the reaction rate over meso-CoO_x was nine times higher than that over meso-Co_3O_4. It is found that the samples with more surface Co^{2+} species possessed better oxygen activation ability, and the Co^{2+} species were the active sites that favored the formation of highly active O_2^- and O_2^{2-} (especially O_2^-) species.

1. Introduction

Most volatile organic compounds (VOCs) are harmful to the environment and human health [1,2]. A number of technologies are available to control VOC emission, such as absorption, adsorption, incineration, photocatalytic oxidation, and catalytic oxidation [3–5]. Catalytic oxidation has been regarded as one of the most promising pathways for the abatement of VOCs due to its high efficiency and low cost [5,6], in which the key issue is the availability of high-performance catalysts. Therefore, it is desirable to fabricate highly active catalysts at low temperatures, thus reducing the high energy consumption for the removal of low-concentration VOCs.

As a typical transition metal oxide, Co_3O_4 attracts much attention due to its excellent reducibility and large amount of oxygen vacancies [7–10]. Since heterogeneous catalysis takes place on the surface of a catalyst, increasing the surface area of a material is beneficial for improving its physicochemical properties, and hence enhancing the catalytic performance. A facile route to obtaining a material with a high surface area is to have the material fabricated in a mesoporous structure. Ordered mesoporous Co_3O_4 (meso-Co_3O_4) networks are usually generated using the nanocasting method with mesoporous silica (e.g., KIT-6, SBA-15, or SBA-16) as a hard template, in which KIT-6 is mostly adopted due to its three-dimensionally ordered mesoporous architecture [11,12]. Previously, our group used the vacuum- or ultrasound-assisted silica-templating strategy to successfully obtain a series of meso-Co_3O_4 materials [13–16] and observed that meso-Co_3O_4 catalysts with high surface areas performed excellently in the oxidation of CO or typical VOCs.

Co_3O_4 possesses a spinel-type crystal structure, in which there are Co^{3+} ions on the octahedral coordination sites and Co^{2+} ions on the tetrahedral coordination sites. It has been reported that Co_3O_4 is highly active for CO oxidation: Its surface Co^{3+} ions are the active site favorable for CO adsorption, whereas its surface Co^{2+} ions with a neighboring oxygen vacancy are easily reoxidized by gas-phase O_2 molecules to form adsorbed oxygen species [17,18]. It is generally accepted that the oxidation of an organic compound takes place via a redox cycle of catalyst on the surface of transition metal oxides, and the organic molecules can react with the chemisorbed oxygen species to yield the total oxidation products [19,20]. Recently, Gu and co-workers fabricated ordered mesoporous CoO by adopting H_2 reduction of nanocast Co_3O_4, and observed that the rock-salt structured CoO showed good catalytic activity for CO oxidation, which was attributed to the oxidation of surface Co^{2+} by oxygen to Co^{3+} [18]. Our previous works have also demonstrated that defective Co_3O_4 (CoO_x) showed high catalytic activity for methane oxidation due to its good methane adsorption ability and improved low-temperature reducibility

* Corresponding authors. Fax: +86 10 6739 1983.
E-mail addresses: yxliu@bjut.edu.cn (Y. Liu), jgdeng@bjut.edu.cn (J. Deng), hxdai@bjut.edu.cn (H. Dai).

http://dx.doi.org/10.1016/j.jcat.2017.05.016
0021-9517/

[21]. CoO exclusively containing Co^{2+} ions in octahedral coordination is generally believed to be inactive for CO oxidation. However, the surface Co^{2+} species are easily oxidized to the Co^{3+} species by gaseous oxygen [22,23], accompanied by the formation of chemisorbed oxygen species. The surface-activated oxygen species are needed to oxidize the VOCs.

Based on these considerations, we here propose a facile reduction process of meso-Co_3O_4 with a glycerol aqueous solution, in which the CoO phase could be gradually formed from the surface to the bulk. As a typical VOC, *o*-xylene was selected to evaluate the catalytic activities of the as-prepared samples. All of the catalysts were characterized by a number of techniques. Effects of the reduction process on the physicochemical properties (such as the texture, crystal phase, surface composition, redox ability, and oxygen activation ability) of cobalt oxides were examined. Differently from CO oxidation, the active sites for VOCs total oxidation over cobalt oxides have seldom been discussed. Hence, the active sites of mesoporous cobalt oxides for *o*-xylene total oxidation are studied.

2. Experimental

2.1. Catalyst preparation

Mesoporous silica (KIT-6) was synthesized adopting the procedures described in the literature [24]. In typical routes, a low HCl concentration (0.5 M) in an aqueous solution using tetraethoxysilane (TEOS, Acros 99%) as silicon source and a mixture of Pluronic P123 and *n*-butanol (Aldrich, 99%) as structure-directing agent. Briefly, 6.0 g of Pluronic P123 was dissolved in 217 mL of deionized water and 9.83 mL of HCl (37%) under vigorous stirring. After complete dissolution, 7.41 mL of *n*-butanol was added. The mixture was stirred at 35 °C for 1 h, and then 13.8 mL of TEOS was slowly added to the homogeneous clear solution. This mixture was further stirred at 35 °C for 24 h, followed by aging at 100 °C for 24 h under static conditions (this process is referred to as hydrothermal treatment). The solid product was filtered, washed several times with deionized water and alcohol, and dried at 100 °C for 24 h. The final KIT-6 template was obtained by calcining the above powders at 550 °C for 4 h in air. Ordered mesoporous Co_3O_4 (meso-Co_3O_4) was fabricated according to the strategy reported previously [15]. The typical fabrication procedures are as follows: After 1.0 g of KIT-6 was suspended in 50 mL of toluene, ultrasonic irradiation (a 100 kHz ultrasonic wave produced at output power 300 W) was applied at room temperature (RT) for 0.5 h. After irradiation, the solution was stirred at 65 °C for 0.5 h, then 2.0 g of $Co(NO_3)_2 \cdot 6H_2O$ was added under vigorous stirring, and finally the solution was dried at 50 °C for 4 h, obtaining pink powders. The pink powders were put into a crucible and then calcined in a muffle furnace at a ramp of 1 °C/min from RT to 600 °C and kept at this temperature for 6 h. The silica template was removed by etching twice with a hot (80 °C) NaOH aqueous solution (2.0 mol/L). The meso-Co_3O_4 sample was obtained after centrifugation, washing three times with deionized water and ethanol, and drying at 80 °C for 24 h.

The ordered mesoporous cobalt oxides were generated by the reduction of meso-Co_3O_4 with glycerol [25]. However, this method, first reported by Schüth and co-workers, had low productivity, thus limiting its wide application. Here, we modify this strategy. The ordered mesoporous cobalt oxides were prepared by adopting a modified meso-Co_3O_4-reduction procedure with glycerol (Scheme 1). The reduction was carried out in a tubular furnace, in which 1.0 g of meso-Co_3O_4 was loaded onto a quartz boat. Before the powders were heated at a ramp of 10 °C/min from RT to 320 °C, a nitrogen flow of 50 mL/min was employed for 0.5 h to remove the O_2 in the system. After the N_2 flow was cut off, a glycerol aqueous solution (50 wt.%) was pumped into the reactor at a rate of 1.0 mL/h with a syringe pump (Longer Pump LSP-01-2A) and evaporated at the outlet of the capillary. The samples obtained after 3 and 12 h of reduction were denoted as meso-CoO_x and meso-CoO, respectively. Afterward, the reactor was kept at 320 °C for 1 h under a nitrogen flow of 50 mL/h to remove the adsorbed species, followed by cooling to RT under the same atmosphere. The brown color of the meso-CoO powders and the absence of CO_2 products formation over meso-CoO during the calcination of meso-CoO suggest that there was no significant carbon accumulation during the reduction process (Fig. S1). Glycerol has a high decomposition temperature (above 290 °C); however, accumulation of carbon was hardly found on the meso-CoO surface at the adopted temperature (320 °C). From the above results, we believe that there was no significant residual glycerol on the sample surface, and it did not influence the total oxidation of *o*-xylene.

All of the chemicals (A.R. in purity) were purchased from Beijing Chemical Reagents Company and used without further purification.

2.2. Catalyst characterization

Physicochemical properties of the mesoporous Co_3O_4, CoO_x, and CoO samples were characterized. X-ray diffraction (XRD) patterns of the samples were obtained on a Bruker D8 Advance diffractometer with CuKα radiation and a nickel filter (λ = 0.15406 nm). Scanning electron microscopic (SEM) images of the samples were recorded on a Gemini Zeiss Supra 55 apparatus (operated at 10 kV). BET (Brunauer–Emmett–Teller) surface areas of the samples were determined via N_2 adsorption at −196 °C on a Micromeritics ASAP 2020 analyzer, with the samples being outgassed at 300 °C under vacuum for 2.5 h before measurement. X-ray photoelectron spectroscopy (XPS, VG CLAM 4 MCD analyzer) was used to determine the binding energies (BEs) of Co2*p*, O1*s*, and C1*s* of surface species, using Mg Kα ($h\nu$ = 1253.6 eV) as excitation source. To remove the adsorbed water and carbonate species on the surface, the samples were pretreated under N_2 (flow rate = 20 mL/min) at 300 °C for 1 h and then cooled to RT. The pretreated samples were degassed in the preparation chamber (10^{-5} Torr) for 0.5 h and then introduced into the analysis chamber (3×10^{-9} Torr) for XPS spectrum recording. The C1*s* signal at 284.6 eV was taken as a reference for BE calibration. Raman spectroscopy (Horiba HR Evolution) was applied to characterize the nature of the catalysts and their adsorbed oxygen species.

Carbon monoxide temperature-programmed reduction (CO-TPR) experiments were carried out on a chemical adsorption analyzer (Autochem II 2920, Micromeritics) coupled with mass spectroscopy (MS) (Hiden QGA). Before TPR measurement, ca. 0.03 g of the sample (40–60 mesh) was loaded into a quartz fixed-bed U-shaped microreactor (i.d. = 4 mm) and pretreated in a N_2 flow of 30 mL/min at 300 °C for 1 h. After being cooled to RT under the same atmosphere, the pretreated sample was exposed to a flow (30 mL/min) of 10% CO–90% Ar (*v*/*v*) mixture and heated from RT to 900 °C at a ramp of 10 °C/min. The alteration in the CO concentration of the effluent was monitored online by the chemical adsorption analyzer. The reduction peak was calibrated against the complete reduction of a known standard, powdered CuO (Aldrich, 99.995%).

Oxygen temperature-programmed desorption (O_2-TPD) was carried out on the same apparatus as that used in the CO-TPR experiments. Prior to O_2-TPD experiment, 30 mg of the sample was preheated under a N_2 flow of 30 mL/min at 300 °C for 1 h. After the sample cooled to RT, an O_2 flow of 40 mL/min was employed for 1 h, and then a He flow of 30 mL/min was used to purge the residual O_2 in the system for 1 h. The O_2 desorption signals were recorded as the sample was heated from RT to 900 °C at a ramp of 10 °C/min and under the same flow. The desorbed amounts of

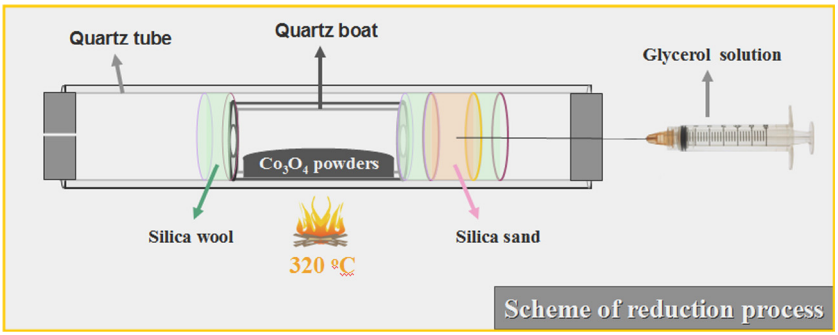

Scheme 1. Illustration of the process of Co_3O_4 reduction.

oxygen were determined according to an oxygen pulse experiment monitored by a thermal conductivity detector together with MS.

In situ diffuse reflectance Fourier transform infrared spectroscopic (DRIFT) experiments were carried on a Nicolet 6700 FT-IR spectrometer with a liquid-nitrogen-cooled MCT detector. Before the experiments, 30 mg of the sample was loaded into a high-temperature IR cell with a KBr window and preheated under a N_2 flow of 30 mL/min at 300 °C for 1 h. Subsequently, the sample was cooled to 240 °C and kept for 0.5 h, and then the background spectrum was recorded. Finally, an air flow (20.0 mL/min) was passed through the IR cell, and the in situ DRIFT spectra of the samples were recorded in an air flow with different times, accumulating 32 scans and a spectrum resolution of 4 cm^{-1}.

2.3. Catalytic activity evaluation

Catalytic activities of the samples were measured in a continuous-flow fixed-bed quartz tubular microreactor (i.d. = 6.0 mm). Before activity measurement, all of the samples were pretreated undera N_2 flow of 20 mL/min at 300 °C for 1 h. To minimize the effect of hot spots, 50 mg of the sample (40–60 mesh) was diluted with 0.25 g of quartz sands (40–60 mesh). The reactant mixture was composed of 1000 ppm *o*-xylene + 20.0 vol% O_2 + N_2 (balance). The 1000-ppm *o*-xylene was generated by passing a N_2 flow through a pure *o*-xylene-containing bottle that was chilled in an isothermal bath at 0 °C. The total flow was 16.6–166.0 mL/min, giving a space velocity (SV) of 20,000–200,000 mL/(g h). Reactants and products were analyzed online by gas chromatography (GC-14C, Shimadzu) with a flame ionization detector (FID) and a thermal conductivity detector (TCD), using a stabilwax-DA column (30 m in length) and a Carboxen 1000 column (3 m in length). The balance of carbon throughout the catalytic system was estimated to be 99.5 ± 1.5%. The *o*-xylene conversion is defined as $(c_{inlet}-c_{outlet})/c_{inlet} \times 100\%$, where the c_{inlet} and c_{outlet} were the inlet and outlet *o*-xylene concentrations in the feed stream, respectively. The absence of a mass transfer limitation under reaction conditions was verified both experimentally and theoretically. The estimation of the Damköhler number under the most unfavorable conditions reveals that the external diffusion mass transfer resistance was negligible. Performing a Weisz–Prater analysis is a facile way to evaluate the absence or presence of internal mass transfer limitation. According to the Weisz–Prater criterion, the dimensionless Weisz–Prater parameter (N_{W-P}) value is less than 0.3, which can be considered a sufficient condition for the absence of significant pore diffusion limitation [26]. When *o*-xylene was oxidized at 230 °C over the meso-CoO_x sample, the N_{W-P} value was calculated to be 0.18, less than 0.3. Effective diffusivity was calculated according to the Maxwell–Gilliland formula and Nusselt number (details of calculations are presented in Supplementary Material). The Damköhler number and Weisz–Prater parameter were calculated under the most unfavorable conditions, and the results reveal that the external and internal diffusion (mass transfer resistance) was negligible under the adopted reaction conditions. In the present work, the concentration of *o*-xylene was low (1000 ppm), and the kinetic calculation was obtained at low *o*-xylene conversions (<11%). The reaction rates and TOFs were also determined under *o*-xylene conversions below 41%. The low *o*-xylene conversions and low *o*-xylene concentration in *o*-xylene total oxidation would be efficient in avoiding heat transfer effects. Furthermore, by varying the flow rates and catalyst mass (at the same SV), the same *o*-xylene conversions were detected over the as-prepared catalysts for *o*-xylene total oxidation at temperatures below 230 °C. Therefore, we believe that there was no significant heat or mass transfer limitation under the adopted reaction conditions. Furthermore, the axial dispersion effect can be neglected at a reactor/particle diameter ratio higher than 10 and a catalyst bed length/particle diameter ratio higher than 50 [27]. In the present work, the above two ratios were 21 and 65, respectively.

3. Results and discussion

Fig. 1 shows the XRD patterns of the samples. The low-angle XRD pattern of Co_3O_4 showed well-resolved diffraction peaks due to the (211) and (332) crystal planes as well as the shoulder peak

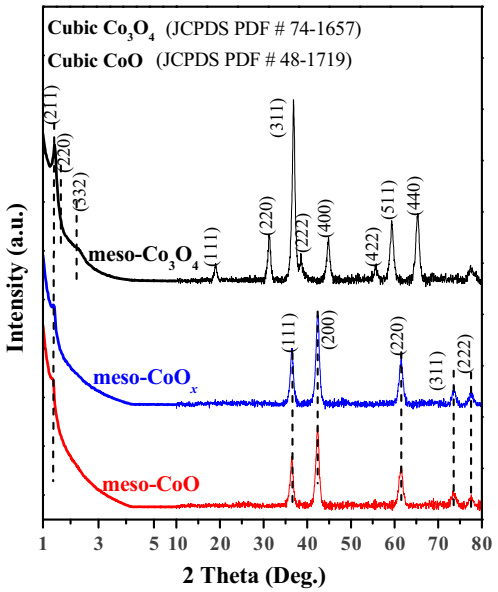

Fig. 1. XRD patterns of the cobalt oxide samples.

due to the (220) crystal plane, which were characteristic of a highly ordered mesoporous structure with a cubic *Ia3d* symmetry. The wide-angle XRD pattern of the Co_3O_4 materials displayed well-resolved reflections that could be indexed to the cubic Co_3O_4 phase (JCPDS PDF# 74-1657). Similar results were reported in one of our previous works [15]. With the extension in reduction time, the mesoporous structure was maintained, but the diffraction peak due to the (332) crystal plane in the low-angle region disappeared (indicating a decrease in structural ordering). It is observed that the XRD pattern of meso-CoO_x was quite similar to that of meso-CoO, implying that a cubic CoO phase (JCPDS PDF # 48-1719) was formed after reduction of Co_3O_4 for 3 h. However, it is hard to determine the amount of the CoO phase formed in the meso-CoO_x sample due to the detection limits of the XRD technique.

Fig. 2A illustrates the CO-TPR profiles of the samples, and their quantitative analysis results are also shown in the figure. There were two main steps of meso-Co_3O_4 reduction, whereas only one peak with a tail was recorded for the reduction of the meso-CoO_x and meso-CoO samples. The reduction band below 300 °C was assigned to reduction of the surface Co^{3+} species, whereas the one above 300 °C was ascribed to reduction of the bulk Co^{3+} and Co^{2+} species [28,29]. A similar reduction profile was observed over the meso-CoO_x and meso-CoO samples. The absence of the reduction signal below 300 °C suggests the presence of only Co^{2+} species in the meso-CoO_x and meso-CoO samples. The broad reduction band with a tail above 300 °C implies a sequential reduction by CO of the bulk Co^{3+} and Co^{2+} species in meso-CoO_x and meso-CoO [29]. To estimate the amounts of different oxygen species, O_2-TPD profiles were recorded, as shown in Fig. 2B. For the meso-Co_3O_4 sample, the weak peaks at 170 and 370 °C were due to the surface-adsorbed oxygen species (O_{WS}) bound to the Co^{2+} and Co^{3+} ions in different coordination environments, whereas the main peak at 795 °C was assignable to the desorption of lattice oxygen from Co_3O_4. Differently from the meso-Co_3O_4 sample, a strong desorption at 430 °C of surface-adsorbed oxygen species (O_{SS}) bound to the Co^{3+} ions (which were generated from Co^{2+} ions by the formation of adsorbed oxygen species in oxygen vacancies) was detected in the meso-CoO_x and meso-CoO samples, and a small peak at 525 or 660 °C was due to the desorption of lattice oxygen from CoO [8,29]. Moreover, a small peak similar to desorption of lattice oxygen from Co_3O_4 at 725 °C was also observed in the meso-CoO_x sample, suggesting the co-presence of Co_3O_4 and CoO in this sample. No apparent desorption of lattice oxygen similar to that from Co_3O_4 was detected in the meso-CoO sample, implying the absence of the Co_3O_4 phase in this sample. In other words, the meso-CoO_x sample was a mixture of Co_3O_4 and CoO, but the sample (meso-CoO) prepared after reduction for 12 h contained a pure CoO phase. The oxygen desorption amounts of the samples are summarized in Table 1. It is obvious that the reduction treatment of meso-Co_3O_4 greatly enhanced the adsorbed oxygen desorption amounts (148.0 μmol/g from meso-CoO_x and 173.1 μmol/g from meso-CoO), which were over 20 times higher than that (7.6 μmol/g) from meso-Co_3O_4. Based on the surface area of the sample, oxygen desorption amounts from the samples were calculated (Table 1). One can clearly observe that the oxygen desorption amount increased with the extension in reduction time (from 0.077 to 1.55, and then to 3.60 μmol/m^2), suggesting that the deeper reduction of the sample resulted in a greater adsorbed oxygen species amount. It should be noted that the surface oxygen species (O_{SS}) bonded to the Co^{3+} species accounted for the higher oxygen amount desorbed from the meso-CoO_x and meso-CoO samples. That is, the surface Co^{2+} would be easily oxidized into Co^{3+} by oxygen molecules, giving rise to formation of the surface oxygen species (O_{SS}) bonded to the Co^{3+} species. Such a high concentration of adsorbed oxygen species on the reduced samples would be beneficial for the redox-involving reactions [17,18].

The porous structures and morphologies of the meso-Co_3O_4, meso-CoO_x, and meso-CoO samples were further examined by the TEM technique, and the results are presented in Fig. 3. It is clearly seen from the TEM images that a well-ordered mesoporous structure was generated in the meso-Co_3O_4, meso-CoO_x, and meso-CoO samples, in good agreement with the low-angle XRD results. This result also demonstrates that the reduction treatment of meso-Co_3O_4 could lead to production of a well-ordered mesoporous CoO. TEM images (Fig. 3c and d) of the meso-CoO_x sample were recorded at different magnifications. There were a number of irregular entities of meso-CoO_x (Fig. 3c), and each entity was composed of ordered mesopores (Fig. 3d). As shown in the high-resolution TEM images of meso-Co_3O_4 and meso-CoO, the intraplanar spacings (*d* values) were measured to be ca. 0.46 and 0.23 nm (Fig. 3b and f), in good consistency with those of the (111) crystal plane of the standard Co_3O_4 (JCPDS PDF# 74-1657) and CoO (JCPDS PDF # 48-1719) samples, respectively. The nitrogen adsorption–desorption isotherm of the meso-Co_3O_4, meso-CoO_x, or meso-CoO sample was a type IV isotherm with a clear H1 hysteresis loop at a relative pressure (p/p_0) of 0.4–0.9 (Fig. 4A), suggesting the presence of uniform mesopores. This result was in good agreement with those of the low-angle XRD and TEM investigations. It is

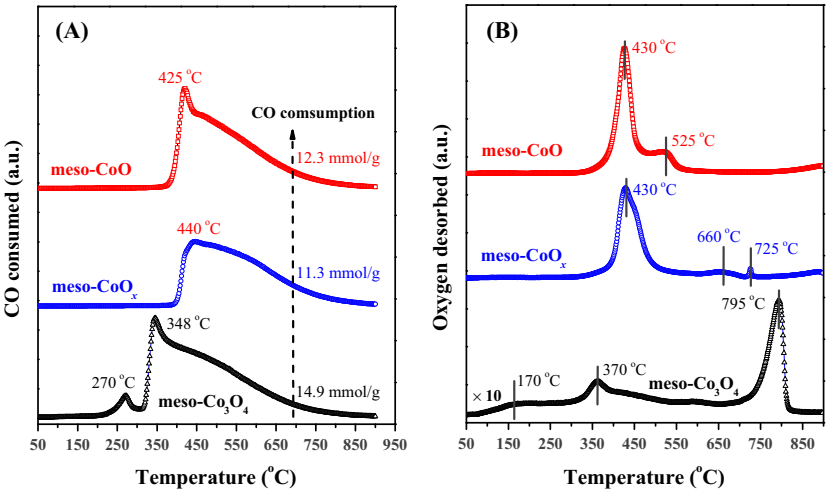

Fig. 2. (A) CO-TPR profiles and (B) O_2-TPD profiles of the cobalt oxide samples.

Table 1
Textural properties and oxygen desorption amounts of the samples.

Sample	Textural property			Oxygen desorption amount	
	Surface area (m^2/g)	Pore diameter (nm)	Pore volume (cm^3/g)	Adsorbed oxygen species ($\mu mol/g$)/($\mu mol/m^2$)	Lattice oxygen species ($\mu mol/g$)/($\mu mol/m^2$)
meso-Co_3O_4	98.1	3.9 and 10.2	0.21	7.6/0.077	16.0/0.16
meso-CoO_x	95.6	3.9 and 7.6	0.17	148.0/1.55	3.8/0.040
meso-CoO	48.1	3.9 and 8.5	0.090	173.1/3.60	30.4/0.63

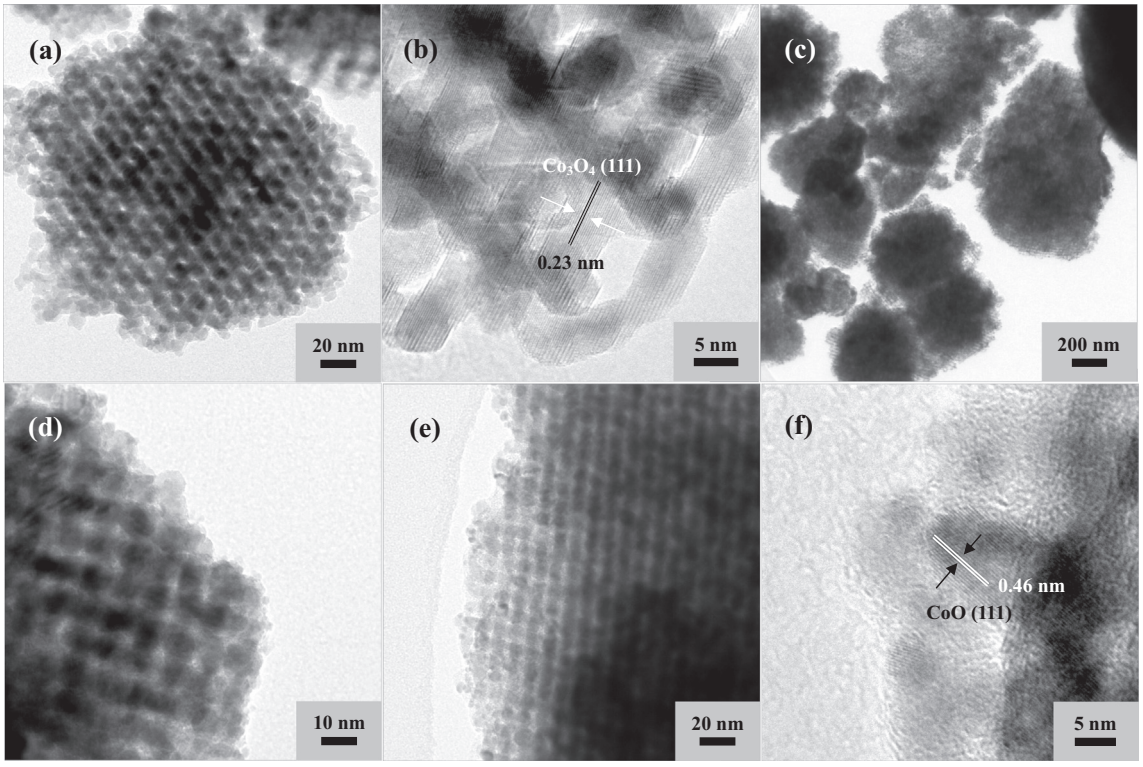

Fig. 3. TEM images of (a, b) meso-Co_3O_4, (c, d) meso-CoO_x, and (e, f) meso-CoO.

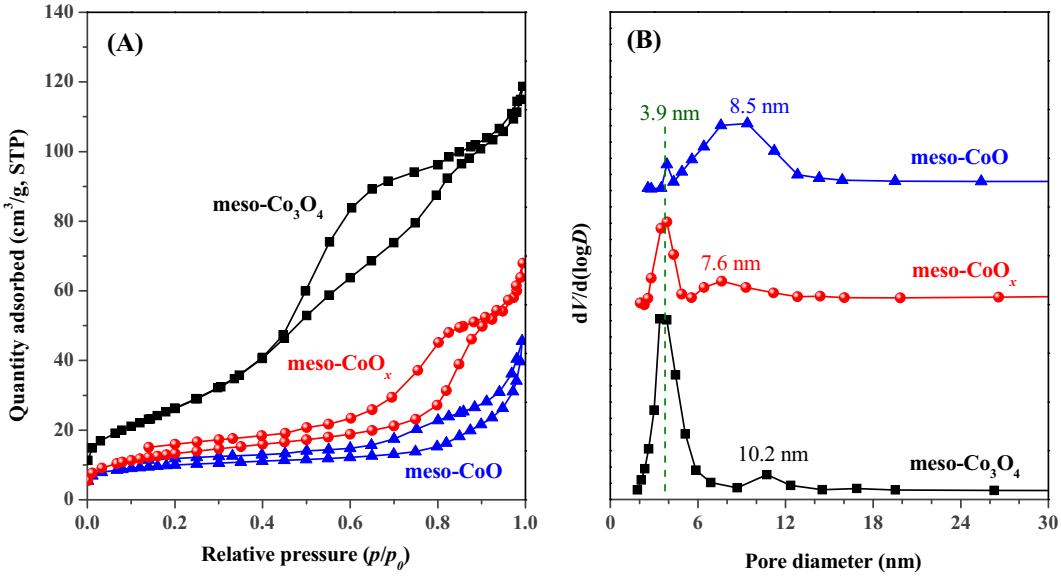

Fig. 4. (A) Nitrogen adsorption–desorption isotherms and (B) pore-size distributions of the cobalt oxide samples.

observed that the capillary condensation step of the CoO sample at slightly higher relative pressures, which might be related to the larger pores, was most likely due to the partial sintering of the mesoporous structure. As shown in Fig. 4B, the pore sizes of the samples were 3.9 and 7.6–10.2 nm. After reduction of the meso-Co_3O_4 sample, the peak at a pore size of 3.9 nm was weakened in intensity, whereas the pore size distribution of the larger pores in the meso-CoO_x or meso-CoO sample was widened. These results were also reflected from the changes in their adsorption–desorption isotherms. Table 1 summarizes the textural parameters of the samples. The BET surface areas of the meso-Co_3O_4, meso-CoO_x, and meso-CoO samples were 98.1, 95.6, and 48.1 m^2/g, respectively. The drop in surface area of the meso-CoO sample might be due to collapse of the smaller pores (3.9 nm).

As a typical VOC, *o*-xylene was selected for evaluating the catalytic activities of the samples. It can be observed clearly from Fig. 5A that *o*-xylene conversion increased with the rise in temperature. The meso-CoO_x and meso-CoO samples performed better than the meso-Co_3O_4 sample. The meso-CoO_x sample showed the best activity at 240 °C (83% *o*-xylene conversion), which was around six times that over the meso-Co_3O_4 sample (13% *o*-xylene conversion at 240 °C). It is understandable that meso-CoO_x performed better than meso-CoO, since the two samples possessed similar surface composition but the latter displayed a smaller surface area. To examine the catalytic stability, we carried out on-stream *o*-xylene oxidation at 240 °C over the meso-CoO_x sample. It is seen from Fig. 5B that no significant loss in activity was observed over meso-CoO_x after 30 h of on-stream reaction. According to the literature [30], CoO could be oxidized easily to Co_3O_4 in air. To investigate the actual temperature for the phase transformation of CoO to Co_3O_4 in air, in situ XRD experiments were carried out on the meso-CoO sample. As shown in Fig. 6, no apparent change in CoO phase was observed with the rise in temperature from RT to 270 °C, but a sudden phase transformation occurred after the temperature rose to 300 °C. These results suggest that the CoO phase in the meso-CoO sample could be oxidized into the Co_3O_4 phase in air above 270 °C, indicating that the CoO phase was stable in air below 270 °C. TEM images (Fig. S2) of the used meso-CoO_x sample were recorded, in which there were no apparent changes in the pore structure after 30 h of on-stream *o*-xylene oxidation at 240 °C. XPS of the used meso-CoO_x sample was also carried out (Fig. S3). Compared with the fresh sample, only slight decreases in surface Co^{2+} and adsorbed oxygen species

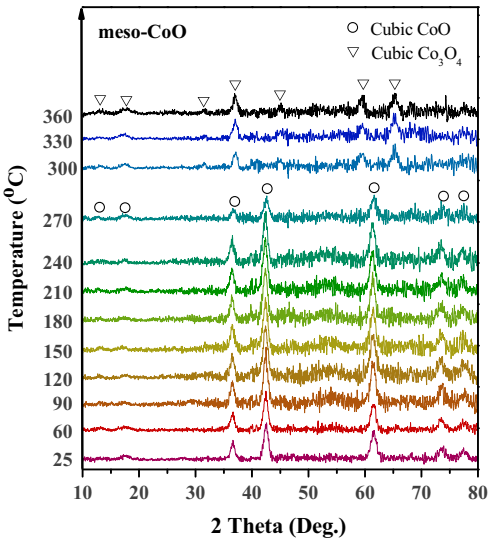

Fig. 6. In situ XRD patterns of meso-CoO at different treatment temperatures in air.

concentrations were observed on the used meso-CoO_x sample (after 30 h of on-stream *o*-xylene oxidation at 240 °C). All of these results suggest that the meso-CoO_x and meso-CoO samples were catalytically stable below 260 °C.

Considering that the surface Co^{2+} species could be oxidized easily into the Co^{3+} species by the gas-phase oxygen molecules (thus generating the active oxygen species) [18,30], it is important to determine the surface element compositions and surface species on the samples. Fig. 7 illustrates the Co2$p_{3/2}$ and O1*s* XPS spectra of the samples, and their surface element compositions are also put in the figure. From Fig. 7A, one can see the Co2$p_{3/2}$ signal of each sample at binding energy (BE) = 779.7 eV, indicative of surface Co^{3+} presence, whereas the Co2$p_{3/2}$ signal at BE = 781.7 eV, together with the shake-up satellite at BE = 786.3 eV, was due to the surface Co^{2+} species [31]. The surface Co^{2+}/Co^{3+} molar ratio (1.22) of meso-CoO_x was similar to that (1.20) of meso-CoO, but much higher than that (0.56) of meso-Co_3O_4. As for the O1*s* XPS spectra (Fig. 7B), one can decompose the asymmetrical O1*s* spectrum of each sample into three components: the surface lattice oxygen (O_{latt}) species at BE = 529.7 eV, the surface-adsorbed oxygen (O_{ads}, O_2^-, O_2^{2-}, or

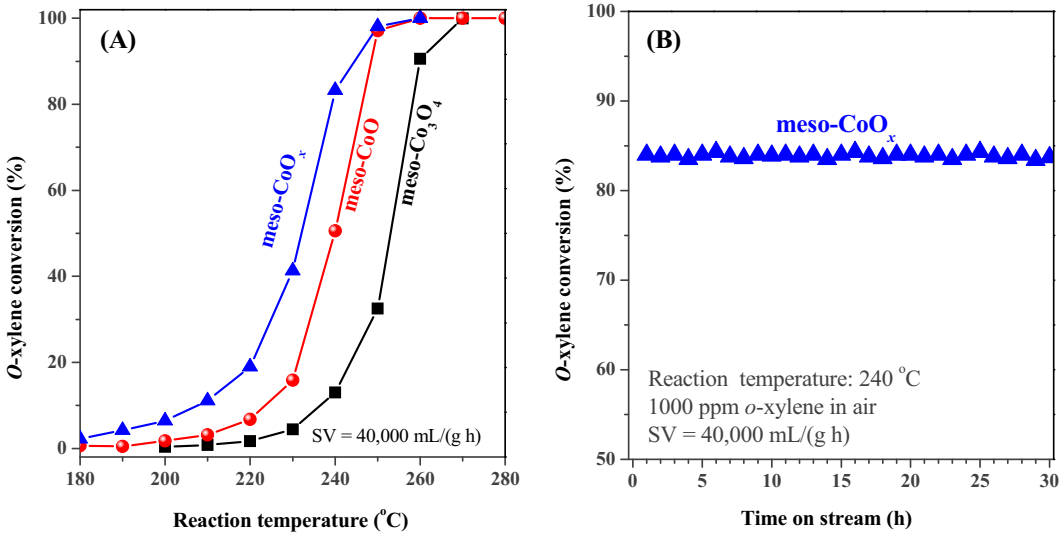

Fig. 5. (A) *O*-xylene conversion as a function of temperature over the cobalt oxide samples and (B) 30 h of on-stream *o*-xylene oxidation over meso-CoO_x.

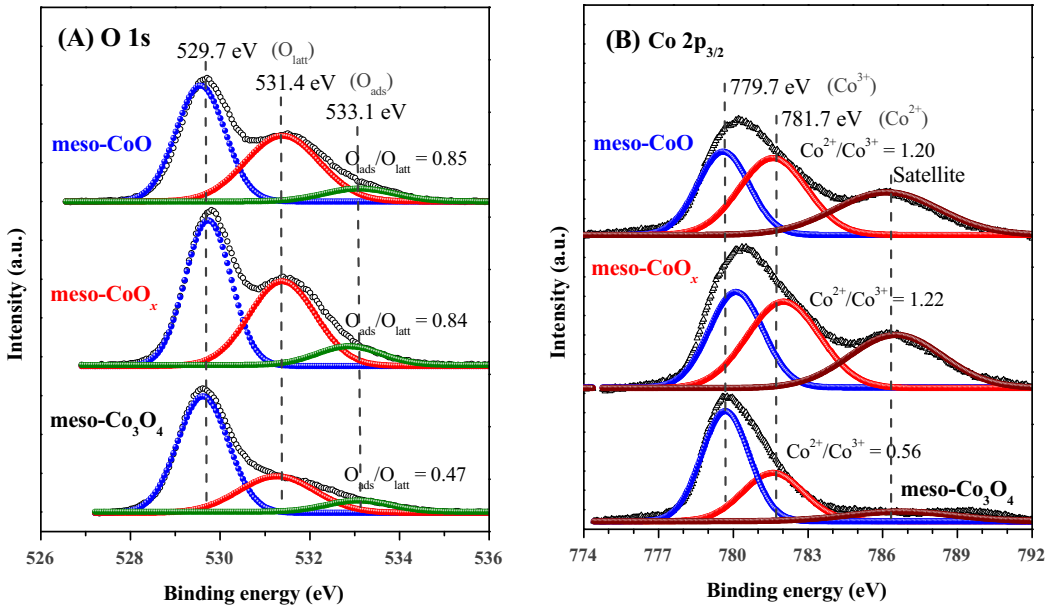

Fig. 7. (A) O1s and (B) Co2$p_{3/2}$ XPS spectra of the cobalt oxide samples.

O^-) species at BE = 531.4 eV, and the surface-adsorbed molecular water at BE = 533.1 eV [15,31]. It is generally believed that the surface-adsorbed oxygen species are active for the oxidation of hydrocarbons at low temperatures [21,32]. It was reported that the catalyst with a higher activation ability for O_2 molecules could show better performance for the combustion of VOCs [32,33]. As shown in Fig. 7B, the surface O_{ads}/O_{latt} molar ratio (0.84) of meso-CoO_x was almost the same as that (0.85) of meso-CoO, but much higher than that (0.47) of meso-Co_3O_4. The XPS results demonstrate that the surface element compositions and surface species were similar on the meso-CoO_x and meso-CoO samples, but the surface Co^{2+} and adsorbed oxygen species concentrations were greatly enhanced after the cobalt oxide samples were reduced for different times. It was understandable that the surface Co^{3+} species over the reduced samples were generated via the oxidation of surface Co^{2+} species by the gas-phase oxygen molecules. That is, a larger surface Co^{2+} species amount would result in formation of a larger amount of the surface-adsorbed oxygen species. The results are in good agreement with those of O_2-TPD investigations. That is, a higher surface Co^{2+} species concentration was more efficient for *o*-xylene oxidation, suggesting that the Co^{2+} species were the active site for *o*-xylene oxidation.

It has been reported that oxidation of VOCs obeys a reaction mechanism of the first order with respect to VOC concentration and the zeroeth order with respect to O_2 concentration under conditions of excess oxygen [15,33–35]. For example, by varying the VOC partial pressure between 0.004 and 0.018 atm and the partial pressure of oxygen between 0.05 and 0.20 atm over the silver-loaded zeolite (HY and HZSM-5) catalysts for the oxidation of butyl acetate under excess oxygen conditions (O_2/butyl acetate molar ratio = 95.5–98.0), Wong and co-workers found that the reaction order with respect to oxygen concentration was close to zero, whereas the reaction order with respect to VOC concentration was close to 1 [34]. Alifanti et al. also claimed that first order with respect to toluene concentration and zeroeth order with respect to oxygen concentration under excessive oxygen conditions (O_2/toluene molar ratio = 117.6) were obtained over the $LaCoO_3/Ce_{1-x}Zr_xO_2$ catalysts for toluene oxidation [35]. Hence, it is reasonably assumed that the oxidation of *o*-xylene at an *o*-xylene/O_2 molar ratio of 1/200 would follow a first-order reaction mechanism with respect to *o*-xylene concentration (*c*): $r = -kc = (-A\exp(-E_a/RT))c$, where *r*, *k*, *A*, and E_a are the reaction rate (mol/s), rate constant (s^{-1}), pre-exponential factor (s^{-1}), and apparent activation energy (kJ/mol), respectively. The *k* values could be calculated from the reaction rates and reactant conversions at different SVs (e.g., 20,000, 40,000, and 80,000 mL/(g h)) and reaction temperatures. To avoid mass transfer limitations, the temperatures used for kinetic calculation were lower than 230 °C, at which the reactant conversions over the samples were below 11%. Fig. S2 shows the Arrhenius plots for *o*-xylene oxidation over the samples, and their apparent activation energies are summarized in Table 2. A highly linear relationship of ln *k* versus reverse reaction temperature was observed from the Arrhenius plots for *o*-xylene oxidation over the as-prepared samples, implying that *o*-xylene oxidation under the present reaction conditions followed a first-order reaction mechanism with respect to *o*-xylene concentration over these samples. The apparent activation energies over meso-CoO_x, meso-CoO, and meso-Co_3O_4 were 105.2 ± 5.4, 100.1 ± 7.3, and 132.1 ± 7.0 kJ/mol (at 95% confidence level), respectively. The E_a values over meso-CoO_x and meso-CoO were rather close, but much lower than that over meso-Co_3O_4 for *o*-xylene combustion. Due to similar surface elemental compositions on meso-CoO_x and meso-CoO, *o*-xylene oxidation would follow similar reaction pathways at the same active sites of the two samples, suggesting that the Co^{2+} species might be the active site for the addressed reaction. Based on the above results, we could accurately calculate the turnover frequencies (TOF) according to the number of surface Co^{2+} sites in the samples. According to the surface atomic configuration of the (111) plane (Fig. S4), there are 21 O^{2-} ions, 9 Co^{3+} ions, and 5 Co^{2+} ions in meso-Co_3O_4, and 2 O^{2-} ions and 9 Co^{2+} ions in meso-CoO and meso-CoO_x. The areas of the illustrated (111) plane in meso-Co_3O_4, meso-CoO, and meso-CoO_x are estimated to be 3.3923 nm^2 (i.e., $(1.414 \times 0.808)^2 \times 0.433 \times 6$), 0.8481 nm^2 (i.e., $(1.414 \times 0.404)^2 \times 0.433 \times 6$), and 0.8481 nm^2 (i.e., $(1.414 \times 0.404)^2 \times 0.433 \times 6$), respectively. The surface areas of meso-Co_3O_4, meso-CoO, and meso-CoO_x were 98.12×10^{18}, 48.09×10^{18}, and 95.56×10^{18} nm^2/g, which were equal to 1.45×10^{20} Co^{2+} ions per gram (0.24×10^{-3} mol/g), 5.10×10^{20} Co^{2+} ions per gram (0.85×10^{-3} mol/g), and 10.14×10^{20} Co^{2+} ions per gram (1.68×10^{-3} mol/g), respectively. The TOF = xC_0/n, where *x* is the

Table 2
Reaction rates, TOFs, *o*-xylene conversions at 240 °C, and apparent activation energies for *o*-xylene oxidation of the samples.

Temperature (°C)	Reaction rate ($\times 10^{-9}$ mol/(g s))			TOF ($\times 10^{-6}$ (s^{-1}))		
	meso-CoO	meso-CoO_x	meso-Co_3O_4	meso-CoO	meso-CoO_x	meso-Co_3O_4
200	8.01	29.24	2.20	9.4	17.4	9.2
210	14.20	50.30	3.70	16.7	30.0	15.4
220	30.60	86.26	7.74	36.0	51.3	32.2
230	71.98	187.64	15.61	84.7	111.7	64.3
Conversion at 240 °C (%)	50.6	83.3	13.0	–	–	–
E_a (kJ/mol)	105.2 ± 5.4	100.1 ± 7.3	132.1 ± 7.0	–	–	–
A (molecule/(g s))	7.9×10^9	9.0×10^9	1.8×10^{12}	–	–	–

conversion at a certain temperature, C_0 (mol/(g s)) is the initial *o*-xylene molar amount per second and per gram (since the catalytic activities of the samples were detected in a continuous flow), and n (mol/g) is the molar amount of the surface Co^{2+} ions per gram. The *o*-xylene oxidation rates can be calculated according to the activity data and mass of the catalyst. For example, according to the activity data obtained over meso-Co_3O_4 at *o*-xylene concentration = 1000 ppm and SV = 40,000 mL/(g h), the C_0, x, and n were 0.454×10^{-6} mol/(g s), 3.4% at 230 °C, and 0.24×10^{-3} mol/g, respectively; hence the TOF obtained over meso-Co_3O_4 at 230 °C was 64.3×10^{-6} s^{-1}. All of the TOFs and reaction rates of the samples are summarized in Table 2. The *o*-xylene oxidation rates at different temperatures over meso-CoO_x were two and nine times higher than those over meso-CoO and meso-Co_3O_4, respectively. The TOF values estimated on the basis of the surface Co^{2+} site were essentially similar for the three samples, implying that the Co^{2+} species were the active sites for *o*-xylene oxidation. The pre-exponential factor (9.0×10^9 molecules/(g s)) obtained over meso-CoO_x was higher than that (7.9×10^9 molecules/(g s)) obtained over meso-CoO; however, the E_a values obtained over both samples for *o*-xylene oxidation were similar (Table 2). This strongly indicates that the difference in reaction rate was solely due to the variation in number of the active sites, and the significantly higher reaction rate over meso-CoO_x could be ascribed to the richness in Co^{2+} active sites on the surface of this sample [17]. All of the above results indicate that the active sites of the cobalt oxide samples for *o*-xylene oxidation were identical (i.e., the Co^{2+} species).

To further determine the nature of the active sites in meso-CoO for *o*-xylene oxidation, we evaluated the catalytic performance of the meso-CoO and meso-Co_3O_4 samples pretreated under different atmospheres. Prior to evaluation, the samples were pretreated under different atmospheres (nitrogen, oxygen, and 10 vol.% CO + 90 vol.% N_2) at 300 °C for 1 h. According to the results of the in situ XRD and CO-TPR tests, one can see that the CoO phase could be oxidized into the Co_3O_4 phase after pretreatment in an air flow at 300 °C for 1 h, and the Co^{3+} species in the meso-CoO and Co_3O_4 samples could be reduced to the Co^{2+} species in a 10 vol.% CO flow. That is, the Co^{2+} species were rich in the samples pretreated in a 10 vol.% CO flow, whereas the amount of the Co^{2+} species decreased in the oxidized meso-CoO sample. As shown in Fig. 8A, similar catalytic activity was observed over the meso-Co_3O_4 sample pretreated in the nitrogen and oxygen flows, but a significant enhancement in activity (a drop of 30 °C in $T_{50\%}$) was detected over the sample pretreated in a CO flow. This result indicates that a larger amount of the Co^{2+} species was beneficial for *o*-xylene oxidation. From Fig. 8B, one can realize that *o*-xylene oxidation was favored to take place on the Co^{2+} sites, since the catalytic activity decreased with the decrease in Co^{2+} concentration in the meso-CoO sample. All of these results again support the conclusion that the Co^{2+} species were the active site for *o*-xylene oxidation.

So far, many authors have focused on the relationship between the formation of oxygen species and the catalytic activity of a sample for VOCs oxidation [6,21,36–40]. It has normally been accepted that surface-adsorbed oxygen species play a key role in the oxidation of VOCs at low temperatures [6,21,36–38], although some researchers proposed that the lattice oxygen in a sample was more active for VOC oxidation than the adsorbed species [39,40]. Considering the total removal of *o*-xylene below 300 °C over the cobalt oxide samples, the active oxygen species might be generated at lower temperatures. Based on the results of O_2-TPD studies, there were two main desorptions of oxygen species from meso-Co_3O_4 at low temperatures, which were related to the surface O_{WS} and O_{SS} species, respectively. However, there was only one desorption of oxygen species at a lower temperature from the meso-CoO_x and meso-CoO samples, which was due to the surface O_{SS} species. That is, the O_{SS} species might be the active oxygen species, since the samples with a larger amount of the O_{SS} species performed much better for *o*-xylene oxidation.

In order to identify the nature of the surface O_{SS} species on the typical samples, the laser Raman technique was used. As shown in Fig. 9, a typical spectrum of Co_3O_4 (A_{1g}: 686 cm^{-1}, F_{2g}: 523 cm^{-1}, F_{2g}: 480 cm^{-1}, E_g: 205 cm^{-1}, and F_{2g}: 145 cm^{-1}) was recorded on the meso-Co_3O_4 sample [9,41,42]. After reduction of meso-Co_3O_4, the Raman signals due to Co_3O_4 were weakened, and the Raman bands were increased in intensity over the meso-CoO sample, implying destruction of the spinel structure. It is obviously seen that there were three new Raman bands at 1182, 1020, and 831 cm^{-1} of the meso-CoO sample, which could be assigned to the superoxide species (O_2^-) and peroxide species (O_2^{2-}) at the one-electron defect site and the peroxide species (O_2^{2-}) [43,44], respectively. These results suggest that the oxygen species adsorbed on meso-CoO were mainly superoxide and peroxide species. In other words, surface Co^{2+} species were beneficial for oxygen activation to form the superoxide and/or peroxide species.

To further understand the different effects of meso-Co_3O_4 and meso-CoO on oxygen activation ability under reaction conditions, an in situ DRIFT experiment was conducted. The in situ DRIFT profiles versus exposure time were recorded over the samples in an air flow at 240 °C, as shown in Fig. 10. As the exposure time increased, there was detection of adsorbed oxygen molecules at 1260 cm^{-1} and peroxide species at 860 cm^{-1} over the meso-Co_3O_4 sample (Fig. 10A), whereas four adsorbed oxygen species were detected over the meso-CoO sample (Fig. 10B). The absorption bands at 1260, 1160–1220, 1000, and 860 cm^{-1} were related to the adsorbed oxygen molecules (O_2), superoxide species (O_2^-), and peroxide species (O_2^{2-}) at the one-electron defect site, and to peroxide species [43–45]. It is obvious that differing from the meso-Co_3O_4 sample, meso-CoO exhibited a superability to activate oxygen molecules to form superoxide species at the *o*-xylene oxidation temperature (240 °C), although meso-Co_3O_4 could also activate oxygen into peroxide species at high temperatures. There were adsorbed oxygen molecules on meso-Co_3O_4, but the superoxide species with a higher concentration existed on meso-CoO. These results suggest that the surface Co^{2+} species would favor the activation of oxygen to form adsorbed oxygen species (especially the

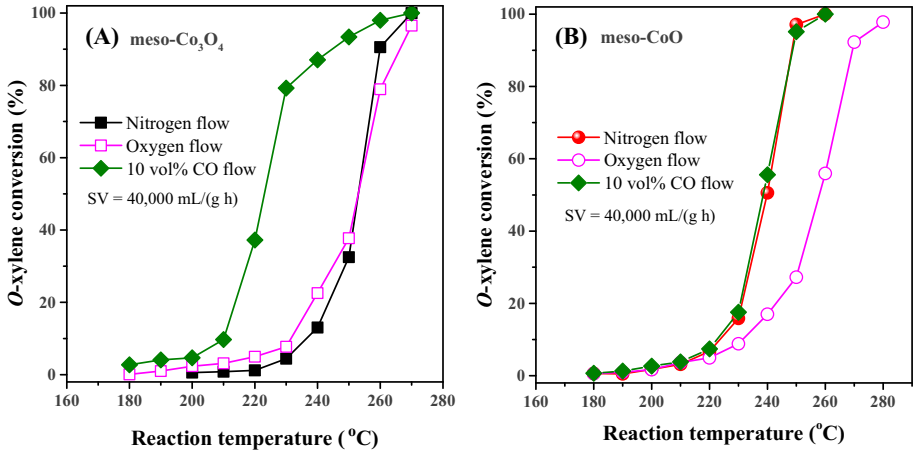

Fig. 8. *O*-xylene conversion as a function of temperature over (A) meso-Co_3O_4 and (B) meso-CoO after pretreatment under different atmospheres at 300 °C for 1 h.

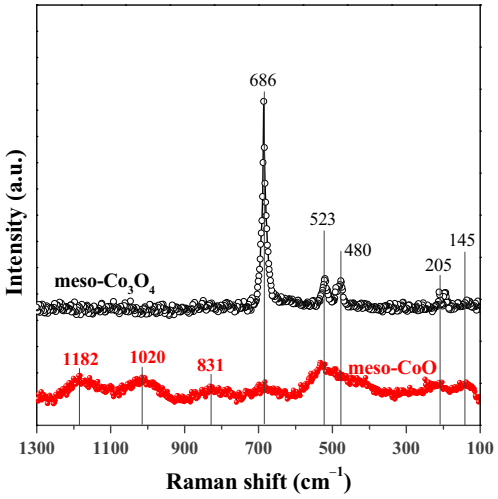

Fig. 9. Raman spectra of the meso-CoO and meso-Co_3O_4 samples.

superoxide species), coinciding with the results of laser Raman investigations. Since the adsorbed oxygen species were easily mutually transformed ($O_2^- \leftrightarrow O_2^{2-}$) on the surface of a catalyst [44], it is hard to elucidate whether the peroxide species were transformed from superoxide species or were directly generated through the activation of oxygen molecules detected by the laser Raman and in situ DRIFT techniques.

In the past several years, a number of studies have focused on the effect of active oxygen species on oxidation reactions. Due to the instability of the monoxide species (O^-), the superoxide species (O_2^-) and peroxide species (O_2^{2-}) at the one-electron defect site were active in the oxidation of CO and hydrocarbons (e.g., propane), and such active oxygen species are usually formed from O_2 molecules on the surface oxygen vacancies of transition metal oxides [10,43–50]. For instance, after studying the reaction mechanism of low-temperature CO oxidation over a TiO_2-supported Au catalyst, Liu and co-workers pointed out that the O_2 species adsorbed onto the oxygen vacancies ($O_{vacancy}$) at the Ti oxide surface were O_2^-, and these superoxide species adjacent to the Au particles were responsible for the catalytic oxidation of CO over the Au/Ti$(OH)_4^*$ catalyst at RT [47]. Schubert and co-workers investigated the effect of support on oxygen supply in CO oxidation over supported Au catalysts and found that the reducible transition metal oxides (e.g., Fe_2O_3) exhibited supercatalytic activity for CO oxidation due to their ability to provide reactive oxygen species. These authors believed that the abundant $O_{vacancy}$ in the vicinity of the gold clusters on the reducible transition metal oxide supports could provide reactive oxygen species involved in the oxidation of CO [50]. Based on the results obtained in the present studies and reported in the literature, the adsorbed oxygen species on meso-Co_3O_4 came from the gas-phase oxygen molecules activated

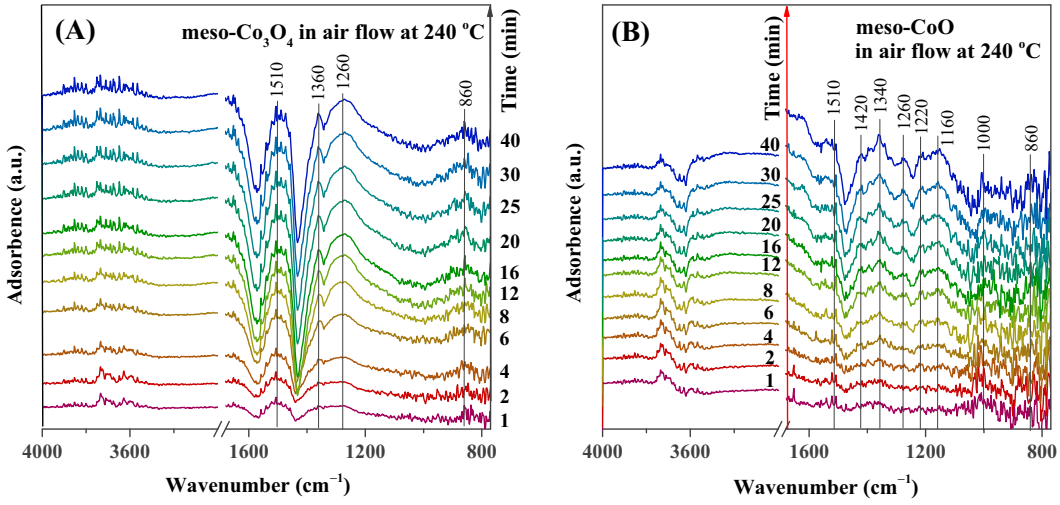

Fig. 10. In situ DRIFT spectra of (A) meso-Co_3O_4 and (B) meso-CoO in a flow of air at 240 °C for different times.

on the surface $O_{vacancy}$ of the cobalt oxide samples. The low surface $O_{vacancy}$ reasonably explains why there was a small amount of adsorbed oxygen species desorption from the meso-Co_3O_4 sample. The ultrahigh amount of adsorbed oxygen species desorption from meso-CoO indicates that there was a large amount of $O_{vacancy}$ in meso-CoO. The $O_{vacancy}$ near the Co^{2+} species could pick up electrons from Co^{2+} to form O_2^- via the pathway $Co^{2+} + O_{vacancy} + O_2 \rightarrow O_2^- + Co^{3+}$ (accompanied by the oxidation of Co^{2+} to Co^{3+}), thus activating the gas-phase O_2 molecules. Therefore, the surface Co^{2+} species were the main center for oxygen activation, which well explains the existence of surface Co^{3+} species (XPS results) and the strong desorption signals of surface oxygen species bound to the Co^{3+} ions (O_2-TPD results) on the meso-CoO_x and meso-CoO samples.

4. Conclusions

meso-CoO_x and meso-CoO samples were prepared via reduction of meso-Co_3O_4 by glycerol at different times, and exhibited high catalytic activities for *o*-xylene oxidation. The meso-CoO_x sample with a surface composition similar to the meso-CoO sample and a surface area similar to the meso-Co_3O_4 sample performed best for *o*-xylene oxidation, giving rise to an *o*-xylene conversion of 83% at 240 °C and a reaction rate nine times higher than that over the meso-Co_3O_4 sample. The good catalytic performance of meso-CoO_x was associated with the Co^{2+} species concentration, which was identified as the active site for *o*-xylene oxidation. The Co^{2+} species were highly active for the activation of gas-phase oxygen molecules to active oxygen species (O_2^- and O_2^{2-}), especially the superoxide species. Our results demonstrate that the surface Co^{2+} species were the main center for oxygen activation. This finding may be useful for the design of novel and high-performance catalysts for oxygen-involving reactions.

Acknowledgments

This work was supported by the NSF of China (21377008, 21677004, and 21477005), the National High Technology Research and Development Program of China (863 Program, 2015AA034603), the Beijing Nova Program (Z141109001814106), the NSF of Beijing Municipal Commission of Education (KM201410005008), and Scientific Research Base Construction–Science and Technology Creation Platform–National Materials Research Base Construction.

Appendix A. Supplementary material

Supplementary data associated with this article can be found, in the online version, at http://dx.doi.org/10.1016/j.jcat.2017.05.016.

References

[1] A.L. Bolden, C.F. Kwiatkowski, T. Colborn, New look at BTEX: are ambient levels a problem?, Environ Sci. Technol. 49 (2015) 5261–5276.
[2] J.Y. Zheng, M. Shao, W.W. Che, L.J. Zhang, L.J. Zhong, Y.H. Zhang, D. Streets, Speciated VOC emission inventory and spatial patterns of ozone formation potential in the pearl river delta, China, Environ. Sci. Technol. 43 (2009) 8580–8586.
[3] F.I. Khan, A.K. Ghoshal, Removal of volatile organic compounds from polluted air, J. Loss Prev. Process Ind. 13 (2000) 527–545.
[4] H.L. Chen, H.M. Lee, S.H. Chen, M.B. Chang, S.J. Yu, S.N. Li, Removal of volatile organic compounds by single-stage and two-stage plasma catalysis systems: a review of the performance enhancement mechanisms, current status, and suitable applications, Environ. Sci. Technol. 43 (2009) 2216–2227.
[5] S.C. Kim, W.G. Shim, Catalytic combustion of VOCs over a series of manganese oxide catalysts, Appl. Catal. B 98 (2010) 180–185.
[6] H.X. Dai, Environmental catalysis: a solution for the removal of atmospheric pollutants, Sci. Bull. 60 (2015) 1708–1710.
[7] Y.F. Wang, C.B. Zhang, F.D. Liu, H. He, Well-dispersed palladium supported on ordered mesoporous Co_3O_4 for catalytic oxidation of *o*-xylene, Appl. Catal. B 142–143 (2013) 72–79.
[8] C.Y. Ma, Z. Mu, J.J. Li, Y.G. Jin, J. Cheng, G.Q. Lu, Z.P. Hao, S.Z. Qiao, Mesoporous Co_3O_4 and Au/Co_3O_4 catalysts for low-temperature oxidation of trace ethylene, J. Am. Chem. Soc. 132 (2010) 2608–2613.
[9] B.Y. Bai, J.H. Li, Positive effects of K^+ ions on three-dimensional mesoporous Ag/Co_3O_4 catalyst for HCHO oxidation, ACS Catal. 4 (2014) 2753–2762.
[10] J. Haber, W. Turvk, Kinetic studies as a method to differentiate between oxygen species involved in the oxidation of propene, J. Catal. 190 (2000) 320–326.
[11] A. Rumplecker, F. Kleitz, E.L. Salabas, F. Schüth, Hard templating pathways for the synthesis of nanostructured porous Co_3O_4, Chem. Mater. 19 (2007) 485–496.
[12] M.B. Zheng, J. Cao, S.T. Liao, J.S. Liu, H.Q. Chen, Y. Zhao, W.J. Dai, G.B. Ji, J.M. Cao, J. Tao, Preparation of mesoporous Co_3O_4 nanoparticles via solid-liquid route and effects of calcination temperature and textural parameters on their electrochemical capacitive behaviors, J. Phys. Chem. C 113 (2009) 3887–3894.
[13] Y.S. Xia, H.X. Dai, H.Y. Jiang, L. Zhang, Three-dimensional ordered mesoporous cobalt oxides: highly active catalysts for the oxidation of toluene and methanol, Catal. Commun. 11 (2010) 1171–1175.
[14] J.G. Deng, L. Zhang, H.X. Dai, Y.S. Xia, H.Y. Jiang, H. Zhang, H. He, Ultrasound-assisted nanocasting fabrication of ordered mesoporous MnO_2 and Co_3O_4 with high surface areas and polycrystalline walls, J. Phys. Chem. C 114 (2010) 2694–2700.
[15] Y.X. Liu, H.X. Dai, J.G. Deng, S.H. Xie, H.G. Yang, W. Tan, W. Han, Y. Jiang, G.S. Guo, Mesoporous Co_3O_4-supported gold nanocatalysts: highly active for the oxidation of carbon monoxide, benzene, toluene, and *o*-xylene, J. Catal. 309 (2014) 408–418.
[16] Z.X. Wu, J.G. Deng, Y.X. Liu, S.H. Xie, Y. Jiang, X.T. Zhao, J. Yang, H. Arandiyan, G. S. Guo, H.X. Dai, Three-dimensionally ordered mesoporous Co_3O_4-supported Au–Pd alloy nanoparticles: high-performance catalysts for methane combustion, J. Catal. 332 (2015) 13–24.
[17] X.W. Xie, Y. Li, Z.Q. Liu, M. Haruta, W.J. Shen, Low-temperature oxidation of CO catalysed by Co_3O_4 nanorods, Nature 458 (2009) 746–749.
[18] D. Gu, C.J. Jia, C. Weidenthaler, H.J. Bongard, B. Spliethoff, W. Schmidt, F. Schüth, Highly ordered mesoporous cobalt-containing oxides: structure, catalytic properties, and active sites in oxidation of carbon monoxide, J. Am. Chem. Soc. 137 (2015) 11407–11418.
[19] S. Ordóñez, L. Bello, H. Sastre, R. Rosal, F.V. Dìez, Kinetics of the deep oxidation of benzene, toluene, *n*-hexane and their binary mixtures over a platinum on γ-alumina catalyst, Appl. Catal. B 38 (2002) 139–149.
[20] C. He, P. Li, J. Cheng, Z.P. Hao, Z.P. Xu, A comprehensive study of deep catalytic oxidation of benzene, toluene, ethyl acetate, and their mixtures over Pd/ZSM-5 Catalyst: mutual effects and kinetics, Water Air Soil Pollut. 209 (2010) 365–376.
[21] S.H. Xie, Y.X. Liu, J.G. Deng, X.T. Zhao, J. Yang, K.F. Zhang, Z. Han, H.X. Dai, Three-dimensionally ordered macroporous CeO_2-supported Pd@Co nanoparticles: highly active catalysts for methane oxidation, J. Catal. 342 (2016) 17–26.
[22] P. Broqvist, I. Panas, H.A. Persson, A DFT study on CO oxidation over Co_3O_4, J. Catal. 210 (2002) 198–206.
[23] J. Jansson, Low-temperature CO oxidation over Co_3O_4/Al_2O_3, J. Catal. 194 (2000) 55–60.
[24] T.W. Kim, F. Kleitz, B. Paul, R. Ryoo, MCM-48-like large mesoporous silicas with tailored pore structure: facile synthesis domain in a ternary triblock copolymer–butanol–water system, J. Am. Chem. Soc. 127 (2005) 7601–7610.
[25] H. Tüysüz, Y. Liu, C. Weidenthaler, F. Schüth, Pseudomorphic transformation of highly ordered mesoporous Co_3O_4 to CoO via reduction with glycerol, J. Am. Chem. Soc. 130 (2008) 14108–14110.
[26] J.R. Paredes, E. Díaz, F.V. Díez, S. Ordóñez, Combustion of methane in lean mixtures over bulk transition-metal oxides: evaluation of the activity and self-deactivation, Energy Fuels 23 (2009) 86–93.
[27] F. Kapteijn, J.A. Moulijn, A. Tarfaoui, Catalyst characterization and mimicking pretreatment procedures by temperature-programmed techniques, Stud. Surf. Sci. Catal. 123 (1999) 525–541.
[28] L. Lukashuk, K. Föttinger, E. Kolar, C. Rameshan, D. Teschner, M. Hävecker, A. Knop-Gericke, N. Yigit, H. Li, E. McDermott, M. Stöger-Pollach, G. Rupprechter, Operando XAS and NAP-XPS studies of preferential CO oxidation on Co_3O_4 and CeO_2-Co_3O_4 catalysts, J. Catal. 344 (2016) 1–15.
[29] Y.B. Yu, T. Takei, H. Ohashi, H. He, X.L. Zhang, M. Haruta, Pretreatments of Co3O4 at moderate temperature for CO oxidation at −80 °C, J. Catal. 267 (2009) 121–128.
[30] X.L. Xu, J.Q. Li, DFT studies on H_2O adsorption and its effect on CO oxidation over spinel Co_3O_4 (110) surface, Surf. Sci. 605 (2011) 1962–1967.
[31] S.H. Xie, J.G. Deng, S.M. Zang, H.G. Yang, G.S. Guo, H. Arandiyan, H.X. Dai, Au–Pd/3DOM Co_3O_4: highly active and stable nanocatalysts for toluene oxidation, J. Catal. 322 (2015) 38–48.
[32] H.Y. Chen, A. Sayari, A. Adnot, F. Larachi, Composition–activity effects of Mn–Ce–O composites on phenol catalytic wet oxidation, Appl. Catal. B 32 (2001) 195–204.
[33] Y. Wang, H. Arandiyan, J. Scott, M. Akia, H.X. Dai, J.G. Deng, K.F. Aguey-Zinsou, R. Amal, High performance Au–Pd supported on 3D hybrid strontium-substituted lanthanum manganite perovskite catalyst for methane combustion, ACS Catal. 6 (2016) 6935–6947.
[34] C.T. Wong, A.Z. Abdullah, S. Bhatia, Catalytic oxidation of butyl acetate over silver-loaded zeolites, J. Hazard. Mater. 157 (2008) 480–489.

[35] M. Alifanti, M. Florea, S. Somacescu, V.I. Parvulescu, Supported perovskites for total oxidation of toluene, Appl. Catal. B 60 (2005) 33–39.
[36] L. Wang, C.B. Zhang, H. He, F.D. Liu, C.X. Wang, Effect of doping metals on OMS-2/γ-Al_2O_3 catalysts for plasma-catalytic removal of *o*-xylene, J. Phys. Chem. C 120 (2016) 6136–6144.
[37] Y.F. Wang, C.B. Zhang, Y.B. Yu, R.L. Yue, H. He, Ordered mesoporous and bulk Co_3O_4 supported Pd catalysts for catalytic oxidation of *o*-xylene, Catal. Today 242 (2015) 294–299.
[38] S.H. Xie, H.X. Dai, J.G. Deng, Y.X. Liu, H.G. Yang, Y. Jiang, W. Tan, A.S. Ao, G.S. Guo, Au/3DOM Co_3O_4: highly active nanocatalysts for the oxidation of carbon monoxide and toluene, Nanoscale 5 (2013) 11207–11219.
[39] H.C. Genuino, S. Dharmarathna, E.C. Njagi, M.C. Mei, S.L. Suib, Gas-phase total oxidation of benzene, toluene, ethylbenzene, and xylenes using shape-selective manganese oxide and copper manganese oxide catalysts, J. Phys. Chem. C 116 (2012) 12066–12078.
[40] Y.S. Wu, M. Liu, Z.C. Ma, S.T. Xing, Effect of alkali metal promoters on natural manganese ore catalysts for the complete catalytic oxidation of *o*-xylene, Catal. Today 175 (2011) 196–201.
[41] H. Shirai, Y. Morioka, I. Nakagawa, Infrared and raman spectra and lattice vibrations of some oxide spinels, J. Phys. Soc. Japan 51 (1982) 592–597.
[42] V.G. Hadjiev, M.N. Iliev, I.V. Vergilov, The Raman spectra of Co_3O_4, J. Phys. C: Solid State Phys. 21 (1988) L199–L201.
[43] J. Guzman, S. Carrettin, A. Corma, Spectroscopic evidence for the supply of reactive oxygen during CO oxidation catalyzed by gold supported on nanocrystalline CeO_2, J. Am. Chem. Soc. 127 (2005) 3286–3287.
[44] R.Q. Long, Y.P. Huang, H.L. Wan, Surface oxygen species over cerium oxide and their reactivities with methane and ethane by means of in situ confocal microprobe Raman spectroscopy, J. Raman Spectrosc. 28 (1997) 29–32.
[45] M. Che, A.J. Tench, Characterization and reactivity of molecular oxygen species on oxide surfaces, Adv. Catal. 32 (1983) 1–148.
[46] A.B. López, K. Krishna, M. Makkee, J.A. Moulijn, Active oxygen from CeO_2 and its role in catalysed soot oxidation, Catal. Lett. 99 (2005) 203–206.
[47] H.C. Liu, A.I. Kozlov, A.P. Kozlova, T. Shido, K. Asakura, Y. Iwasawa, Active oxygen species and mechanism for low-temperature CO oxidation reaction on a TiO_2-supported Au catalyst prepared from $Au(PPh_3)(NO_3)$ and as-precipitated titanium hydroxide, J. Catal. 185 (1999) 252–264.
[48] Q. Fu, H. Saltsburg, M.F. Stephanopoulos, Active nonmetallic Au and Pt species on ceria-based water-gas shift catalysts, Science 301 (2003) 935–938.
[49] B.G. Świerkosz, Nano-Au/oxide support catalysts in oxidation reactions: provenance of active oxygen species, Catal. Today 112 (2006) 3–7.
[50] M.M. Schubert, S. Hackenberg, A.C. Veen, M. Muhler, V. Plzak, R.J. Behm, CO oxidation over supported gold catalysts—"Inert" and "Active" support materials and their role for the oxygen supply during reaction, J. Catal. 197 (2001) 113–122.